Bursting dynamics due to a homoclinic cascade in Taylor–Couette flow

J. ABSHAGEN[1], J. M. LOPEZ[2], F. MARQUES[3] AND G. PFISTER[1]

[1]Institute of Experimental and Applied Physics, University of Kiel, 24105 Kiel, Germany
[2]Department of Mathematics and Statistics, Arizona State University, Tempe, AZ 85287, USA
[3]Departament de Física Aplicada, Universitat Politècnica de Catalunya, 08034, Barcelona, Spain

Transitions between regular oscillations and bursting oscillations that involve a bifurcational process which culminates in the creation of a relative periodic orbit of infinite period and infinite length are investigated both experimentally and numerically in a short-aspect-ratio Taylor–Couette flow. This bifurcational process is novel in that it is the accumulation point of a period-adding cascade at which the mid-height reflection symmetry is broken. It is very rich and complex, involving very-low-frequency states arising via homoclinic and heteroclinic dynamics, providing the required patching between states with very different dynamics in neighbouring regions of parameter space. The use of nonlinear dynamical systems theory together with symmetry considerations has been crucial in interpreting the laboratory experimental data as well as the results from the direct numerical simulations. The phenomenon corresponds to dynamics well beyond the first few bifurcations from the basic state and so is beyond the reach of traditional hydrodynamic stability analysis, but it is not fully developed turbulence where a statistical or asymptotic approach could be employed. It is a transitional phenomenon, where the phase dynamics of the large-scale structures (jets of angular momentum emanating from the boundary layer on the rotating inner cylinder) becomes complicated. Yet the complicated phase dynamics remains accessible to an analysis of its space–time characteristics and a comprehensive mechanical characterization emerges. The excellent agreement between the experiments and the numerical simulations demonstrates the robustness of this complex bifurcation phenomenon in a physically realized system with its inherent imperfections and noise. Movies are available with the online version of the paper.

1. Introduction

Beyond the primary instability in fluid dynamic problems, which typically have more than one governing parameter (e.g. parameters characterizing the ratios of forces, such as the Reynolds number, and geometric parameters), subsequent instabilities can often be understood in terms of more complicated codimension-two bifurcations (Guckenheimer 1984) which act as organizing centres for the local nonlinear dynamics in the multi-dimensional parameter space (Mullin 1993). At such bifurcations, several eigenmodes compete and complex dynamics and chaos are common, for example in local Takens–Bogdanov, fold–Hopf and Hopf–Hopf bifurcations. Associated with these bifurcations one often encounters global bifurcations, such as homoclinic/heteroclinic collisions. Other global bifurcations
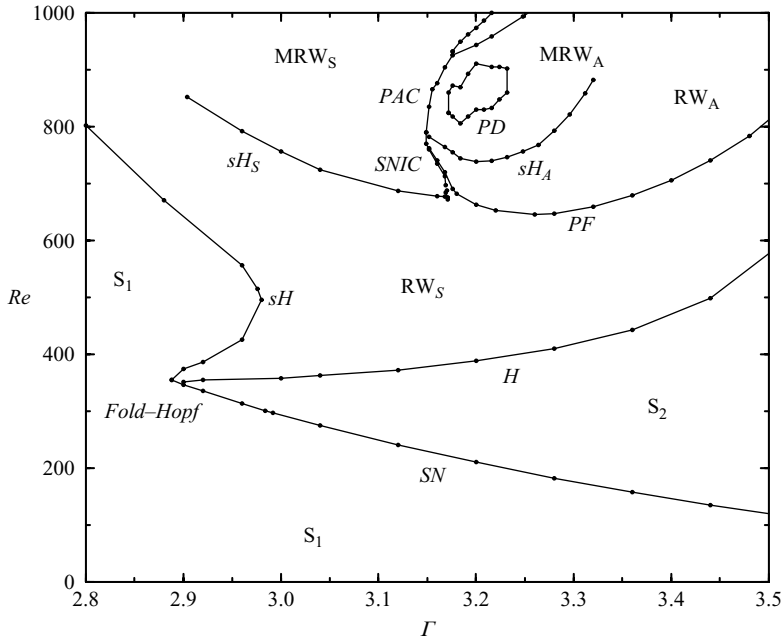
FIGURE 1. Experimentally determined (Abshagen 2000) bifurcation curves separating the different regimes observed; the prominent stable state in each region is labelled in typeface roman and the bifurcation curves are labelled in typeface italic.

involve a large region of phase space and are not as amenable to a local analysis via normal forms. These include the *SNIC* (saddle-node of fixed points on an invariant curve) bifurcation, the blue-sky bifurcation (saddle-node of cycles on an invariant curve), and Feigenbaum period-doubling cascades.

A well-known hydrodynamic system displaying a large variety of different dynamics, including most of the aforementioned bifurcations, is Taylor–Couette flow. A nice feature of this system is that it is an enclosed flow in a simple geometry, which allows very precise experiments and numerical simulations. In particular, the experiments of Abshagen (2000) offer very detailed experimental results in a range of parameters exhibiting a large variety of dynamics, as can be seen in figure 1. The figure shows experimentally determined bifurcation curves in the aspect ratio–Reynolds number (Γ, Re) parameter space for a Taylor–Couette flow with the inner cylinder rotating and the outer cylinder and both endwalls stationary. The dynamics in the region of parameter space shown are organized by several codimension-two bifurcations.

The experimental techniques and numerical methods used in this paper are summarized in §2 and §3. These have already been used in the analysis of different but related problems (Lopez & Marques 2003; Lopez, Marques & Shen 2004; Abshagen *et al.* 2005*a*, *b*; Lopez & Marques 2005; Marques & Lopez 2006), and only the salient aspects are presented.

Section 4 summarizes previously known results in this problem, for Reynolds numbers below 800. For moderate Reynolds numbers (up to 400), the dynamics are organized by the codimension-two fold–Hopf bifurcation, where a saddle-node bifurcation curve *SN* and a Hopf bifurcation curve *H* intersect. Below the saddle-node curve there exists a stable axisymmetric state, S_1, with a single jet of angular momentum coming off the boundary layer on the inner cylinder at the mid-plane;

above the curve another stable solution, S_2, appears. This is an axisymmetric state with two jets symmetric about the mid-plane; S_1 and S_2 are depicted in figure 4. Both states coexist and there is hysteretic behaviour between them around the saddle-node curve (*SN* in figure 1). The details are described in §4.1.

The two-jet state S_2 undergoes a number of subsequent bifurcations that are analysed in this paper. It undergoes a symmetry-breaking Hopf bifurcation H, leading to a rotating wave state, RW_S, with azimuthal wavenumber $m = 1$; this is described in §4.2. The rotating wave is Z_2-symmetric: it is invariant under the action of a reflection about the geometric centre of the cylinders; this central reflection is also called an inversion. For small aspect ratios, the rotating wave undergoes a secondary Hopf bifurcation sH_S to a modulated rotating wave MRW_S, described in §4.3. The spatial Z_2-symmetry of RW_S becomes a space–time Z_2 symmetry of MRW_S. For large aspect ratios, the inversion symmetry is broken in a pitchfork bifurcation (*PF*) resulting in asymmetric rotating waves RW_A and RW'_A, described in §4.4. The transition between the symmetric and non-symmetric bifurcated solutions, described in §4.4, occurs along the *SNIC* bifurcation curve in figure 1. This curve emerges from a narrow parameter region of complex dynamics, where the sH_S and *PF* bifurcation curves meet, described in §4.4. These results have already been described in Abshagen *et al.* (2005*a*, *b*). Note that the rotating waves, RW_S and RW_A, are fixed points (equilibria) in a rotating reference frame precessing around the cylinder axis at a convenient angular speed (i.e. rotating with the precession frequencies of the rotating waves). Analogously, the modulated rotating wave MRW_S becomes a limit cycle in the appropriate precessing frame. As such, rotating waves are also called relative equilibria, and modulated rotating waves are called relative periodic orbits. We adopt this point of view here and consider the characteristics of these relative solutions that are independent of the reference frame considered, effectively filtering out the precession frequency. These characteristics are introduced in §4, and consist of the amplitude and relative phase of the jets emanating from the inner cylinder due to centrifugal instability.

Bifurcations of limit cycles (RW_S and RW_A) and relative limit cycles (MRW_S and MRW_A) play an important role in the present study, and it is useful to list all the possible isolated codimension-one bifurcations that a limit cycle may undergo. There are seven of these bifurcations†. Four of them are local, i.e. they are bifurcations of fixed points of ordinary differential equations (ODEs) or maps, and can be analysed in detail from the corresponding normal form. They are: the Hopf bifurcation, where the limit cycle collapses into a fixed point; the cyclic fold (saddle-node) bifurcation, where the limit cycle collides with an unstable periodic orbit and vanishes; the period-doubling or flip bifurcation where a multiplier of the orbit crosses the unit circle through -1; and the secondary Hopf (or Neimark–Sacker) bifurcation where a pair of complex-conjugate multipliers cross the unit circle, and the limit cycle becomes a quasi-periodic solution on an invariant torus. All of these bifurcations are present in the problem under consideration in this paper.

The remaining three bifurcations of limit cycles are global, and the period of the limit cycle grows unbounded as the bifurcation point is approached. They are:

(*a*) The collision of the limit cycle with an external saddle fixed point, the saddle-loop homoclinic (*SLH*) bifurcation; the saddle exists before and after the bifurcation

---

† They are described in many books on dynamical systems, e.g. Shil'nikov *et al.* (2001), Kuznetsov (2003), and at `http://www.scholarpedia.org/article/Blue-sky_catastrophe` maintained by A. Shil'nikov and D. Turaev.

and its eigenvalues do not change sign in the process. The limit cycle's length remains finite and its period becomes unbounded as $\log(1/|\mu|)$, where μ is the distance in parameter space from the bifurcation.

(*b*) The occurrence of a saddle-node bifurcation (of fixed points) on an invariant curve (*SNIC* bifurcation). The saddle appears at the bifurcation point, and has a zero eigenvalue at the bifurcation. Following the bifurcation, a pair of fixed points, one stable and the other unstable, exists on the invariant curve. The limit cycle's length remains finite and its period becomes unbounded as $1/\sqrt{(|\mu|)}$.

(*c*) The occurrence of a saddle-node bifurcation of cycles on an invariant curve (the blue-sky bifurcation). On approaching the bifurcation point, the limit cycle starts to revolve around the ghost of the saddle-node of cycles, increasing both its period and its length. At the bifurcation point, both the period and length of the limit cycle become infinite.

The blue-sky bifurcation has only been studied relatively recently. The question about the possible existence of a periodic orbit bifurcation with its period and length increasing without bound was raised by Palis & Pugh (1974). It was confirmed in 1995 by Turaev & Shil'nikov (1995) and Shil'nikov & Turaev (1997), who then provided a simple low-dimensional example (Shil'nikov & Turaev 2000). Subsequently, examples of blue-sky bifurcations have been found in model problems in fluid dynamics, such as in two-dimensional binary convection (Meca *et al.* 2004). Note, however, that some authors have used the term blue-sky inaccurately, referring to a variety of different global bifurcations of limit cycles, including the aforementioned isolated global bifurcations of limit cycles in which the cycle's length remains finite (i.e. *SLH* and *SNIC* bifurcations).

In this paper, new numerical simulations and experiments at larger Reynolds numbers ($Re \gtrsim 800$) are analysed in §5. Both the experiments and the numerics reveal a very rich array of dynamics which are not amenable to normal form analysis. The asymmetric rotating wave RW_A undergoes a secondary Hopf bifurcation sH_A to a modulated rotating wave MRW_A, described in §5.1. The transition between the symmetric and non-symmetric bifurcated solutions now involves MRW_S and MRW_A, and it is much more complicated than the *SNIC* bifurcation found at lower Reynolds numbers. It consists of a cascade of heteroclinic collisions of MRW_S with external saddles, each collision increasing the period and length of the relative limit cycle. At the accumulation point of this period-adding cascade (the *PAC* curve in figure 1), the MRW_S has infinite period and length, and disappears. At the same point, the stable MRW_A appears, also with infinite period but finite length. This process is described in §5.2 and §5.3. At these large Reynolds numbers ($Re \gtrsim 800$), additional bifurcations take place, such as period-doubling bifurcations (*PD*) of MRW_A, and chaos at even higher Reynolds numbers ($Re \gtrsim 1000$).

As the period-adding cascade of homoclinic bifurcations takes place in a narrow parameter range, it may be very sensitive to small imperfections and noise in the experiments. In the *PAC* region, both imperfections and noise play a role in the interpretation of the experimental results. The experiments have very precise control of temperature and angular velocities of the cylinders, as described in §2. Nevertheless, the temperature and angular velocities experience small random drifts (below the level of uncertainty in experimental measurements), resulting in small variations in Re (and in the aspect ratio Γ to a lesser extent). These drifts are effectively observed as noise. Close to the accumulation point of the *PAC*, these small variations result in a drift of the experimental state between the distinct periodic solutions that accumulate in the *PAC*. In this regime, the experimentally observed state is no longer periodic,

but instead exhibits characteristics of intermittency and bursting driven by the small random drifts in the control parameters. This is explained in detail in §5.4.

The Z_2 reflection symmetry about the cylinder mid-plane is slightly broken by small inherent imperfections in the experimental apparatus (Abshagen 2000). It is well-known that systems with Z_2 symmetry are particularly sensitive to imperfections, both when Z_2 is purely spatial (Benjamin 1978*a*, *b*; Benjamin & Mullin 1981; Crawford & Knobloch 1991; Moehlis & Knobloch 1998; Knobloch & Moehlis 1999) as well as when the Z_2 symmetry is a space–time symmetry (Abshagen, Pfister & Mullin 2001; Marques, Lopez & Iranzo 2002). In some parameter ranges near the *PAC*, the influence of the imperfections has indeed been observed, resulting in a preference for one of the MRW$_A$ following the bifurcation. This is explained in detail in §5.5. The Taylor–Couette flow is hence seen as an extremely rich, well-defined hydrodynamics problem in which to investigate the influence of imperfections and noise on the nonlinear dynamics, and in particular to determine to what extent the observed dynamics in the experiments are deterministic or due to the inevitable and ubiquitous presence of noise in the physical experiment.

2. Experimental technique

The experimental setup of the Taylor–Couette system used for this study consists of a fluid (silicon oil with kinematic viscosity $\nu = 10.2$ mm^2 s^{-1} at a nominal temperature of 21°C, with an absolute uncertainty of ± 0.1 mm^2 s^{-1}) confined in the gap between two concentric cylinders. The outer cylinder and the top and bottom endwalls were held fixed. A phase-locked loop circuit controlled the angular velocity of the inner cylinder, Ω, to an accuracy of better than one part in 10^{-4} in the short-term and 10^{-7} in the long-term average. The inner cylinder was machined from stainless steel with radius $r_i^* = 12.50 \pm 0.01$ mm, while the outer cylinder, with $r_o^* = 25.00 \pm 0.01$ mm, was made from optically polished glass. The apparatus was located in an air-controlled cabinet and the laboratory was air conditioned. The temperature of the fluid was thermostatically controlled to 21.00 ± 0.01°C. The uncertainty in the temperature contributes a relative uncertainty in the viscosity of about 0.0025 mm^2 s^{-1} (given by the variation of viscosity with temperature at 21°C times the uncertainty in temperature). The absolute uncertainty in viscosity produces a 1% uncertainty in the absolute value of the Reynolds number. However, the relative uncertainty in Re due to the temperature uncertainty (i.e. the relative uncertainty in the viscosity) is much smaller, of order 0.01%. This is of the same order as the short-term uncertainty in the angular frequency achieved by the phase-locked loop control.

The distance between the endwalls, h, is adjustable via a precision microscrew to within an accuracy of 0.01 mm. In order to decouple the experimental setup from vibrations it is mounted on an optical table. Laser Doppler velocimetry (LDV) was used for measurements of the local flow velocity and laser light-sheet techniques were used for flow visualization. Further technical details of the experimental apparatus and measurement procedures can be found in Gerdts *et al.* (1994) and von Stamm *et al.* (1996). A schematic and a photograph of the apparatus are shown in figure 2.

3. Navier–Stokes equations and the numerical scheme

Consider an incompressible flow confined in an annulus of inner radius r_i^* and outer radius r_o^* and length h, driven by the constant rotation of the inner cylinder at Ω rad s^{-1}. The system is non-dimensionalized using the gap, $d = r_o^* - r_i^*$, as the length
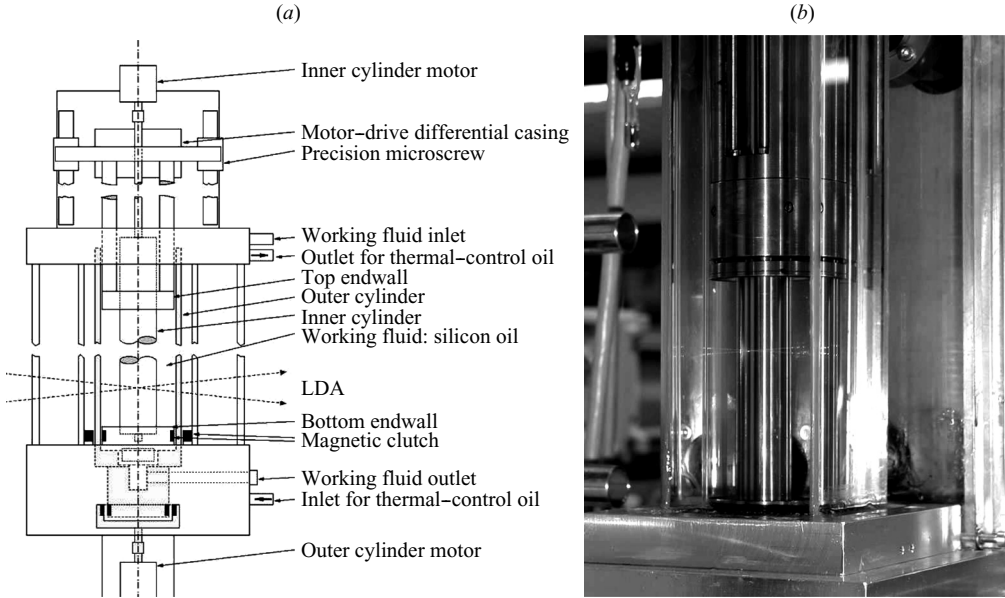
— Inner cylinder motor

— Motor–drive differential casing
— Precision microscrew

— Working fluid inlet
— Outlet for thermal–control oil
— Top endwall
— Outer cylinder
— Inner cylinder
— Working fluid: silicon oil

LDA

— Bottom endwall
— Magnetic clutch

— Working fluid outlet
— Inlet for thermal–control oil

— Outer cylinder motor

FIGURE 2. (*a*) Schematic and (*b*) photo of the experimental apparatus.

scale and the diffusive time across the gap, d^2/ν, as the time scale. The equations governing the flow are the Navier–Stokes equations together with initial and boundary conditions. In cylindrical coordinates, (r, θ, z), we denote the non-dimensional velocity vector and pressure by $\boldsymbol{u} = (u, v, w)$ and p, respectively. The system is governed by three non-dimensional parameters: the radius ratio $\eta = r_i^*/r_o^*$, the annulus aspect ratio $\Gamma = h/d$, and the Reynolds number $Re = \Omega d r_i^*/\nu$. Since the experimental apparatus has radius ratio $\eta = 0.5$, we consider only this value in the numerical simulations.

The non-dimensional Navier–Stokes equations are

$$\partial_t \boldsymbol{u} + (\boldsymbol{u} \cdot \nabla)\boldsymbol{u} = -\nabla p + \nabla^2 \boldsymbol{u}, \qquad \nabla \cdot \boldsymbol{u} = 0, \qquad (3.1)$$

and the no-slip boundary conditions are $u = v = w = 0$ on all stationary boundaries, i.e. at the outer cylinder, $r = r_o = r_o^*/d = 1/(1 - \eta) = 2$, and the top and bottom endwalls $z = \pm 0.5h/d = \pm 0.5\Gamma$, while on the rotating inner cylinder, $r = r_i = r_i^*/d = \eta/(1 - \eta) = 1$, $u = w = 0$ and $v = Re$.

To solve (3.1), a stiffly stable semi-implicit second-order projection scheme is used, where the linear terms are treated implicitly while the nonlinear terms are explicit (see Lopez & Shen 1998; Lopez, Marques & Shen 2002, for more details). For the space variables, we use a Legendre–Fourier approximation. More precisely, the azimuthal direction is discretized using a Fourier expansion with $2N_\theta + 1$ modes corresponding to azimuthal wavenumbers $m = 0, 1, 2, \dots N_\theta$, while the axial and radial directions are discretized with a Legendre expansion. The spectral convergence of the code has already been extensively described for related problems (Lopez & Marques 2003; Lopez *et al.* 2004; Lopez & Marques 2005; Marques & Lopez 2006) as well as in Abshagen *et al.* (2005*a*), where the same flow was computed and compared with the experiments up to $Re \approx 780$. The results presented here at $Re = 830$ have the highest resolution used in that previous study, specifically 48 and 96 Legendre modes in the
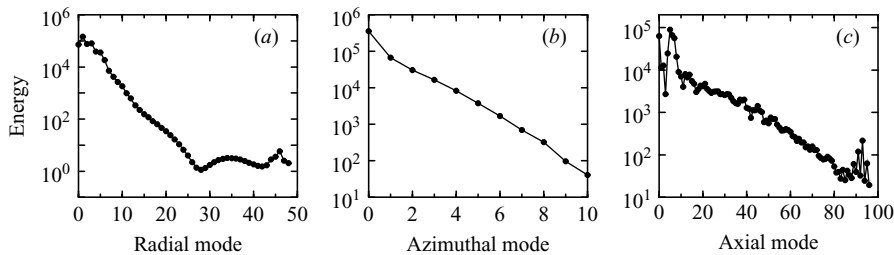
FIGURE 3. Energy ($\mathcal{L}^2$-norm) norm of the spectral modes in the radial (a), azimuthal (b) and axial (c) directions, for a modulated rotating wave solution at $Re = 830$ and $\Gamma = 3.16319$.

radial and axial directions, respectively, $N_\theta = 10$ Fourier modes, and a time-step of $\delta t = 2 \times 10^{-5}$.

Care needs to be taken when solving a system with discontinuous boundary conditions using spectral methods. The jump discontinuities in the azimuthal velocity v where the rotating inner cylinder and the stationary endwall meet need to be regularized in order to avoid spurious numerical oscillations (Gibb's phenomenon) and ensure spectral convergence. In our code, we replace the $v = 0$ boundary condition on the stationary endwalls at $z = \pm 0.5\Gamma$ with

$$ v = Re \exp\left[-\left(\frac{r - r_i}{\epsilon} \right)^2 \right], \tag{3.2} $$

where ϵ is a small parameter that mimics the small gaps between the rotating inner cylinder and the stationary endwall (we have used $\epsilon = 0.005$). See Lopez & Shen (1998) for further details of the use of this regularization in a spectral code.

The spectral convergence of the code has been checked by measuring the kinetic energy (i.e. the $\mathcal{L}^2$-norm) of the spectral modes in the radial, azimuthal and axial directions. Figure 3 shows plots of the spectral energies in one of the more complex cases computed, the seven-loop solution in figure 16, at parameter values $Re = 830$ and $\Gamma = 3.16319$. The figure shows a decay of at least three orders of magnitude in the energy of the spectral modes in the three directions: (a) radial, (b) azimuthal, and (c) axial. With regard to temporal resolution, we note that the precession period of the solutions is the fast time scale of the flow and that it is not dynamically important (see §4.3). The precession period is of order 10^{-2} viscous times, so that we are computing with about 10^3 time-steps per precession period. The slow time scale which characterizes the complex dynamics being analysed here corresponds to the modulation period and it is of the order of the viscous time, and so we have about 10^5 time steps per modulation period; the dynamics reported here are adequately resolved.

The symmetry of the system has important implications for its dynamics. The system is invariant to rotations R_α about the axis and to reflections K_z about the mid-height $z = 0$. The actions of the $SO(2)$ symmetry generated by R_α and the Z_2 symmetry generated by K_z on the velocity are

$$ R_\alpha(u, v, w)(r, \theta, z, t) = (u, v, w)(r, \theta + \alpha, z, t), \tag{3.3} $$

$$ K_z(u, v, w)(r, \theta, z, t) = (u, v, -w)(r, \theta, -z, t). \tag{3.4} $$

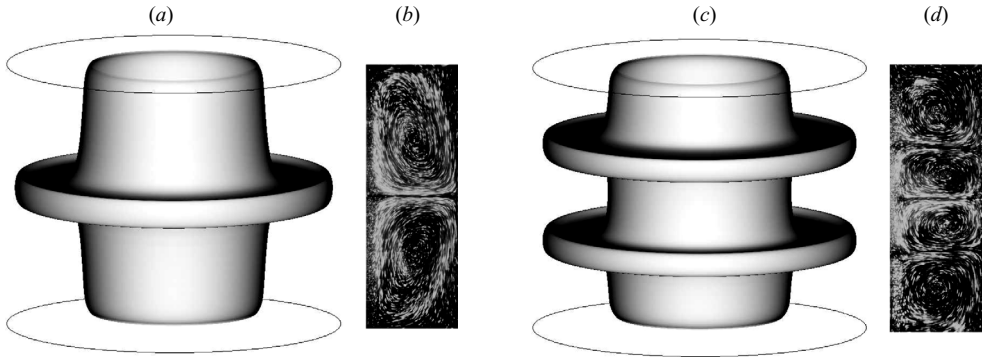The symmetry group of the system is $\mathcal{G} = SO(2) \times Z_2$.

FIGURE 4. S_1, the one-jet state: (*a*) computed isosurface of angular momentum at $rv = 220$ and (*b*) visualization of the experimental flow. S_2, the two-jet state: (*c*) computed isosurface at $rv = 185$ and (*d*) the experimental flow. Both states coexist and are stable at $\Gamma = 3.00$, $Re = 330$ and $\eta = 0.5$.

4. Background results at low *Re*

The experimentally observed regimes and the bifurcation curves separating them in the parameter region $\Gamma \in [2.8, 3.5]$ and $Re \in [0, 1000]$ are shown in figure 1. We have already described the regimes and bifurcation curves below $Re = 800$ in previous studies, and the present paper is focused on $Re \in [800, 1000]$ where very rich and complex dynamics develop just before the onset of turbulence. In order to place these new results in context, a brief description of the previous results is presented first. During the description, new tools for an appropriate analysis of the solutions at large *Re* will be introduced. In particular, these include tools appropriate for the characterization of the slow dynamics associated with the jets of angular momentum and their relative phase.

4.1. *The basic axisymmetric one- and two-jet states, S_1 and S_2*

For very slow rotations ($Re \lesssim 10$), the angular momentum introduced by the rotating inner cylinder is redistributed by viscous dissipation. As *Re* is increased, the angular momentum builds up into a boundary layer on the rotating inner cylinder and is redistributed into the interior by jets erupting from the boundary layer. For $Re \sim 100$ and $\Gamma \sim 3$, there are two Z_2-symmetric steady axisymmetric states: one has a single jet of angular momentum which erupts from the inner cylinder boundary layer at mid-height $z = 0$ (the steady state S_1), and the other has a pair of axisymmetric jets erupting symmetrically about $z = 0$ (the steady state S_2). The meridional recirculations driven by the jets produce the familiar Taylor vortex flows. Isosurface plots of angular momentum for S_1 and S_2 at a point in parameter space where they are both stable ($Re = 330$, $\Gamma = 3.0$, $\eta = 0.5$), along with visualizations of the corresponding experimental flows, are shown in figure 4. The competition between S_1 and S_2 is organized by a codimension-two cusp bifurcation, where two codimension-one curves of saddle-node bifurcations meet, at $Re = 76$, $\Gamma = 3.81$, off to the far right of the region shown in figure 1. The details of the cusp bifurcation have been described in detail elsewhere (Abshagen *et al.* 2005*a,b*; Lopez & Marques 2005). For the range $\Gamma \in [2.8, 3.5]$ considered in this study, S_1 remains stable to large *Re*, and we focus on the fate of S_2 for $Re \in [800, 1000]$.
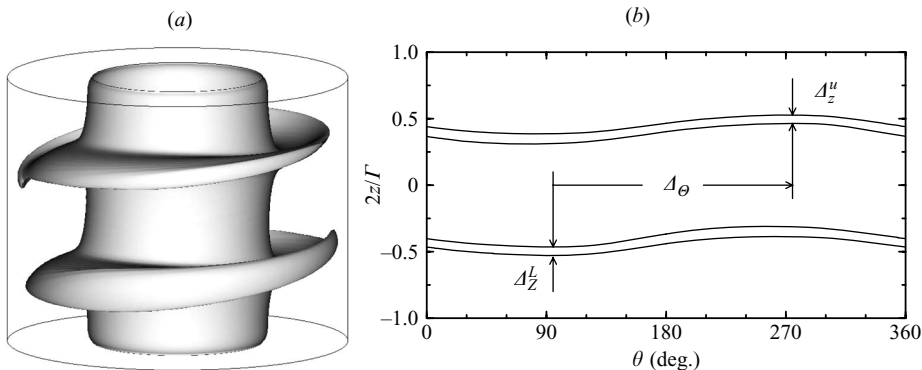
FIGURE 5. (*a*) Isosurface of axial angular momentum at $rv = 320$ for RW$_S$ at $\Gamma = 3.15$ and $Re = 700$, and (*b*) corresponding contours of rv in a (θ, z) section at $r = r_i + 0.3d$ with $v = 0.4Re$. The tilt of the jets is out of phase by $\Delta_{\Theta} = 180°$ and their thickness is $\Delta_Z^U = \Delta_Z^L = 0.0634$.

4.2. *The symmetric rotating wave RWs*

For $\Gamma \in [2.9, 3.5]$, S$_2$ is born at a saddle-node bifurcation *SN* with $Re \approx 200$. The *SN* bifurcation curve is shown in figure 1. On increasing Re to about 400, S$_2$ becomes unstable via a supercritical symmetry-breaking Hopf bifurcation H in which the flow loses its axisymmetry as the two jets in S$_2$ tilt and begin to precess, resulting in a rotating wave RW$_S$ with azimuthal wavenumber $m = 1$ (figure 5a shows an angular-momentum isosurface plot of RW$_S$). The flow is steady in a reference frame rotating with the precession frequency ω_p; for this reason rotating waves are also called *relative equilibria*. The tilt of the jets breaks the mid-height reflection symmetry K_z, but since the tilts are in phase, RW$_S$ has a different Z_2 symmetry consisting of a reflection about $z = 0$ together with a π rotation about the axis, i.e. RW$_S$ is invariant under $K_0 = R_\pi \circ K_z$, which is a reflection about the origin, whose action is

$$K_0(u, v, w)(r, \theta, z, t) = (u, v, -w)(r, \theta + \pi, -z, t). \tag{4.1}$$

Figure 5(*b*) shows contours of the axial angular momentum rv in a (θ, z) planar rendering of an r-constant cylindrical surface for the same RW$_S$ in figure 5(*a*). The values of the radius and the azimuthal velocity of the contour plot are $r = r_i + 0.3d$ and $v = 0.4Re$, giving $rv = 0.52Re$. The tilt of the jets results in two almost sinusoidal shapes. The intensity of the two jets can be quantitatively estimated by measuring the thickness of the upper and lower jets, Δ_Z^U and Δ_Z^L, at the location closest to the corresponding endwall. We can also measure the angular difference between these two locations, Δ_{Θ}, as illustrated in figure 5(*b*). In order to compare different solutions, we will always use the same values $v = 0.4Re$ and $r = r_i + 0.3d$. The K_0 symmetry of RW$_S$ results in $\Delta_Z^U = \Delta_Z^L$, and $\Delta_{\Theta} = 180°$. Note that the phase difference Δ_{Θ} is independent of the precession frequency of RW$_S$ as it is the same in any rotating reference frame. As we shall see, the complex dynamics we analyse in this paper can be completely characterized in terms of the phase Δ_{Θ}.

Figure 1 shows that the bifurcation curves *SN* and H meet at a codimension-two fold–Hopf point at about $(\Gamma, Re) = (2.89, 3.54)$. As is typical for the dynamics in the neighbourhood of a fold–Hopf point, a Neimark–Sacker bifurcation curve also emanates from the fold–Hopf point (Guckenheimer 1984; Guckenheimer & Holmes 1997; Kuznetsov 2003). Note that all the Neimark–Sacker bifurcations found in
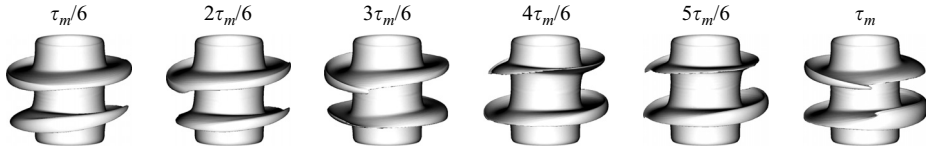
$\tau_m/6$ $2\tau_m/6$ $3\tau_m/6$ $4\tau_m/6$ $5\tau_m/6$ τ_m

FIGURE 6. Isosurfaces of axial angular momentum for MRW_S over one modulation period, at $\Gamma = 3.14$ and $Re = 830$. The isosurface value is $rv = 380$. Movie 1, available with the online version, shows an animation of this sequence.

this study are secondary Hopf bifurcations from relative equilibria, and hence are not generic Neimark–Sacker bifurcations; in particular, they do not have the usual frequency-locking phenomena (Rand 1982; Krupa 1990). Hence, we shall refer to these bifurcations as secondary Hopfs. The codimension-two fold–Hopf bifurcation admits a number of different dynamical scenarios in its neighbourhood, depending on the particulars of the system. From both experimental and numerical results, Abshagen *et al.* (2005*a*) showed that the secondary Hopf bifurcation *sH* is a subcritical bifurcation at which RW_S loses stability as a modulated rotating wave (a relative periodic orbit) is born, but it also is unstable due to the subcriticality of the bifurcation. The result is that to the left of the *sH* curve (i.e. to lower Γ), there are no stable states local to the fold–Hopf bifurcation and the flow evolves towards the far-off stable S_1.

4.3. *The symmetric modulated rotating wave MRWs*

On increasing Re beyond 600, RW_S undergoes further instabilities. For $\Gamma \lesssim 3.15$, the tilted jets of RW_S develop a modulation in their precession which is half a period out of phase between the two jets. This instability is a supercritical secondary Hopf bifurcation sH_S in which the relative equilibrium RW_S loses stability and a stable *relative periodic orbit* MRW_S is spawned. The modulated rotating wave MRW_S is a quasi-periodic solution with two frequencies, but one of these corresponds to the precession frequency ω_p of the underlying RW_S and plays no dynamic role in the bifurcation. The other (modulation) frequency corresponds to the period $\tau_m = 2\pi/\omega_m$ over which the tilted jets oscillate in and out of phase relative to each other. The precession period (over the range of parameters considered) is about 0.03% of the viscous time d^2/ν, whereas the modulation period is at least one viscous time and becomes unbounded in critical regions of parameter space. In a frame of reference precessing with frequency ω_p, MRW_S is time periodic and possesses a spatio-temporal symmetry S corresponding to a temporal evolution of $\tau_m/2$ together with a K_0 reflection (Abshagen *et al.* 2005*a*,*b*). The action of S on the velocity in the precessing frame is

$$S(u, v, w)(r, \theta, z, t) = (u, v, -w)(r, \theta + \pi, -z, t + \tau_m/2). \qquad (4.2)$$

Isosurface plots of the axial component of the angular momentum, rv, in the precessing frame of reference at six phases of the modulation period τ_m are shown in figure 6. The upper and lower jets undergo oscillations in the axial and azimuthal directions. In the first two snapshots, the upper jet carries more angular momentum than the lower jet, occupying a larger portion of the axial span of the cylinders. Half a period later, the situation is reversed (compare isosurfaces at phases $\tau_m/6$ and $2\tau_m/6$ with those at $4\tau_m/6$ and $5\tau_m/6$). In between, the two jets either slide up ($3\tau_m/6$) or down ($6\tau_m/6$) in the axial direction. Movie 1, available with the online version of the paper, is an animation of the sequence in figure 6. Figure 7 shows the
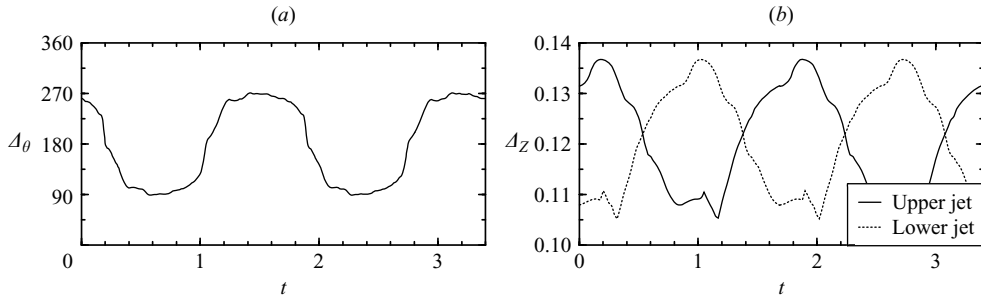
FIGURE 7. Variation with time of (a) the phase difference Δ_Θ and (b) the jet thicknesses Δ_Z^U and Δ_Z^L, for MRW_S at $\Gamma = 3.14$ and $Re = 830$.
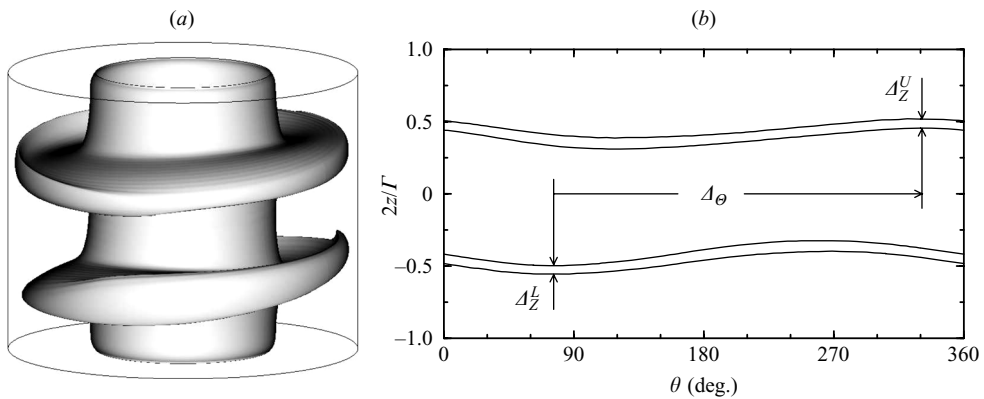

FIGURE 8. (a) Isosurface of axial angular momentum at $rv = 320$ for RW_A at $\Gamma = 3.20$ and $Re = 700$, and (b) corresponding contours of rv in a (θ, z) section at $r = r_i + 0.3d$ with $v = 0.4Re$. The tilt of the jets is out of phase by $\Delta_\Theta = 255°$ and their thickness is $\Delta_Z^U = 0.0641$ and $\Delta_Z^L = 0.0583$.

evolution of the jet thicknesses and relative phase during two modulation periods. The qualitative impressions observed in the movie are now clearly quantified. The relative phase Δ_Θ between the two jets, shown in figure 7(a), is no longer constant at $180°$: it shows little variation for one third of the modulation period during which $\Delta_\Theta \approx 260° = 180° + 80°$, then moves rapidly to $\Delta_\Theta \approx 100° = 180° - 80°$, where it remains for about another third of the period, jumps back to $\Delta_\Theta \approx 260°$, and repeats the cycle. The intensity of the jets also increases and decreases during the modulation period, as shown in figure 7(b).

4.4. *The asymmetric rotating wave RW_A*

For $\Gamma \gtrsim 3.15$, RW_S loses stability at a pitchfork bifurcation PF; the jets become tilted with their tilt angles out of phase, but they continue to precess uniformly. This bifurcation breaks the reflection about the origin K_0 and results in a pair of asymmetric rotating waves, RW_A and RW'_A, related by K_0. The spatial structure of RW_A is illustrated by an angular momentum isosurface plot in figure 8(a), and figure 8(b) shows contours of rv in a (θ, z) planar rendering of an r-constant cylindrical surface for the same solution. The two jets have different intensities, with the upper jet
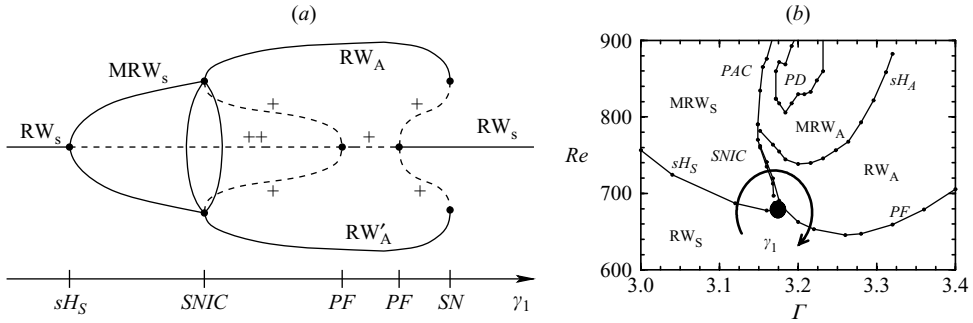
FIGURE 9. (*a*) Schematic bifurcation diagram for the transition between regular oscillations (RW$_A$) and bursting dynamics (MRW$_S$) involving a *SNIC* bifurcation and a pitchfork bifurcation, along the path γ_1 depicted in (*b*).

stronger than the lower jet ($\Delta_Z^U = 0.0641$ and $\Delta_Z^L = 0.0583$); the opposite is true for the conjugate state RW$_A'$. The phase difference is no longer 180°, instead $\Delta_\Theta = 255°$ for RW$_A$ and $\Delta_\Theta = 360° - 255° = 105°$ for RW$_A'$.

For $\Gamma > 3.22$, the pitchfork bifurcation *PF* producing RW$_A$ and RW$_A'$ is supercritical, whereas for $\Gamma < 3.22$, *PF* is subcritical producing a pair of unstable rotating waves which subsequently undergo saddle-node bifurcations with RW$_A$ and RW$_A'$. The important point is that these saddle-node bifurcations take place simultaneously *on* MRW$_S$. Looked at another way, as Γ increases toward 3.15 from below, the modulation period of MRW$_S$ grows without bound as saddle-nodes (a pair of them due to the Z_2 symmetry) develop on it, destroying MRW$_S$ and leaving the stable RW$_A$ and RW$_A'$ and their (unstable) saddle partners, together with the heteroclinic connections between them. This is an *SNIC* bifurcation where saddle-nodes develop on a relative periodic orbit (MRW$_S$). A schematic of this bifurcation is presented in figure 9(*a*), where the rotating waves are shown as (relative) equilibria and the modulated rotating wave as a (relative) periodic orbit. The + signs indicate the number of eigenvalues with positive real part of the relative equilibria RW$_S$ and RW$_A$. The one-dimensional path parameterized by γ_1 is shown as a thick arc with an arrow in parameter space in figure 9(*b*). The only feature not computed numerically in the bifurcation diagram is the secondary pitchfork bifurcation of the unstable RW$_S$, whose presence is necessary in order to account for the two eigenvalues with positive real part appearing at the secondary Hopf bifurcation sH_S, and also to provide the unstable RW$_A$ and RW$_A'$ branches appearing at the *SNIC* bifurcation. The bifurcation curves sH_S and *PF* do not collide at a single point but, rather, all the bifurcations depicted in figure 9(*a*) collapse in on a very small region in parameter space shown as a hatched circle in figure 9(*b*) that has been described in detail in Abshagen *et al.* (2005*a*). The *SNIC* bifurcation takes place for $690 \lesssim Re \lesssim 790$ along the curve labelled *SNIC* at about $\Gamma \approx 3.15$ (see figure 1 and the close-up in figure 9*b*). This bifurcation curve separates the symmetric solutions (MRW$_S$ for smaller Γ) from the asymmetric solutions (RW$_A$ and RW$_A'$ for larger Γ). The time intervals over which Δ_Θ essentially remains constant, i.e. the quiescent phases, for MRW$_S$ shown in figure 7, become increasingly longer as Γ is increased toward the infinite-period *SNIC* bifurcation. Following the bifurcation, Δ_Θ does not change any more, remaining at one or the other of the quiescent values that corresponds to the fixed constant Δ_Θ of RW$_A$ or RW$_A'$.
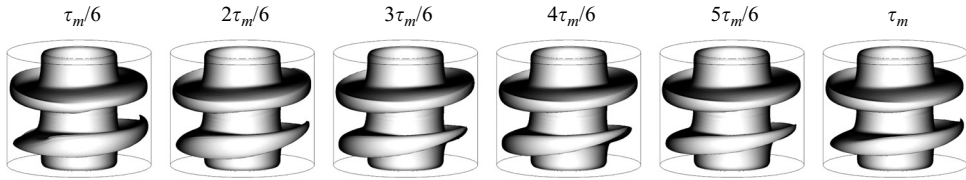
FIGURE 10. Isosurfaces of axial angular momentum for $\mathrm{MRW_A}$ over one modulation period, at $\Gamma = 3.17$ and $Re = 830$. The isosurface value is $rv = 370$. Movies 2 and 3, available with the online version, show animations of this sequence.
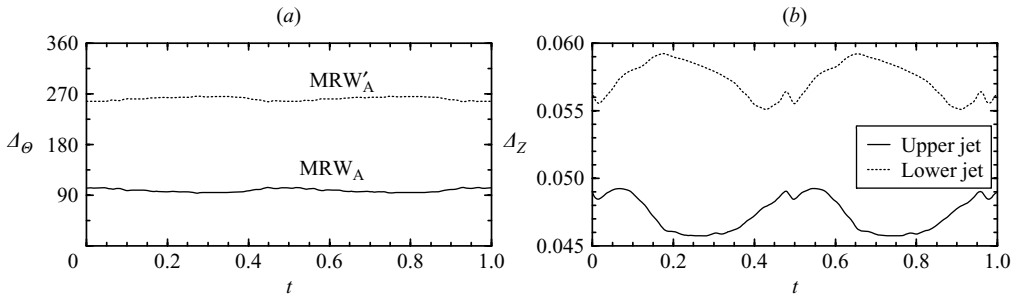

FIGURE 11. Temporal variations of (*a*) the phase differences for $\mathrm{MRW_A}$ (solid curve) and $\mathrm{MRW'_A}$ (dotted curve), and (*b*) the jet widths for $\mathrm{MRW_A}$, all at $\Gamma = 3.17$ and $Re = 830$.

5. New results at high *Re*

5.1. *The asymmetric modulated rotating waves MRW_A and MRW'_A*

For $Re \gtrsim 740$, the rotating waves $\mathrm{RW_A}$ and $\mathrm{RW'_A}$ develop modulations via a supercritical secondary Hopf bifurcation sH_A, giving rise to a pair of asymmetric modulated rotating waves $\mathrm{MRW_A}$ and $\mathrm{MRW'_A}$. The sH_A bifurcation curve becomes tangential to the $SNIC$ bifurcation curve at about $Re = 790$, at which point the $SNIC$ and sH_A bifurcations cease to exist. For $Re \gtrsim 790$, the transition between symmetric and asymmetric solutions no longer occurs at a $SNIC$ bifurcation. Instead, the transition between the asymmetric solutions $\mathrm{MRW_A}$ and $\mathrm{MRW'_A}$ and the symmetric $\mathrm{MRW_S}$ takes place along the symmetry-breaking curve labelled PAC in figure 9(*b*). This transition is much more complicated than the $SNIC$ bifurcation, involving a bifurcational process that is the primary object of the present study.

As is the case with $\mathrm{MRW_S}$, the quasi-periodic $\mathrm{MRW_A}$ and $\mathrm{MRW'_A}$ are also periodic in a frame of reference rotating at their precession frequency. The modulation period is comparable to the viscous time, and becomes unbounded as the $SNIC$ curve is approached; in comparison, the precession period is only about 0.03% of the viscous time. Figure 10 shows isosurface plots of angular momentum over one modulation period of $\mathrm{MRW_A}$ in the precessing frame. Movie 2, available with the online version of the paper, is an animation of this sequence, and movie 3 shows it in a stationary frame of reference.

For $\mathrm{MRW_A}$, both jets undergo modulated oscillations in the azimuthal direction, with the phase difference oscillating around a mean value $\Delta_\Theta \approx 98.5°$ (Δ_Θ for $\mathrm{MRW'_A}$ is 360° minus that for $\mathrm{MRW_A}$) and a peak-to-peak amplitude of the azimuthal modulation of about 10°, as illustrated in figure 11(*a*). Moreover, the lower jet is thicker during the first half of the modulation period (shown in the first three snapshots of figure 10) than in the second half (shown in the last three snapshots of
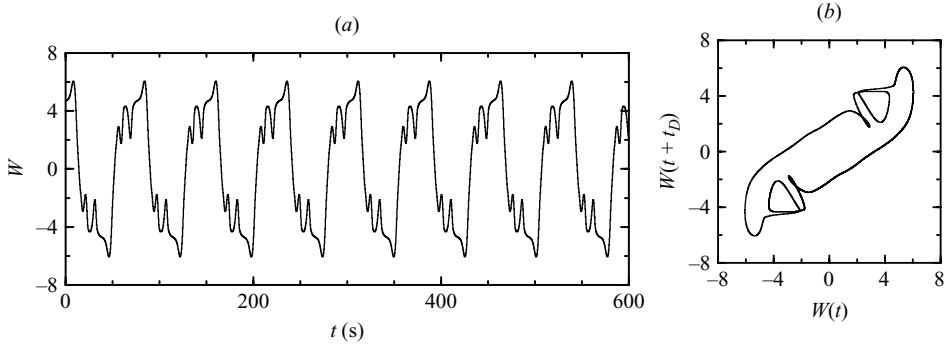
FIGURE 12. (*a*) Low-pass-filtered time-series of the numerically computed axial velocity W for the MRW$_\mathrm{S}$ at $\Gamma = 3.16205$ and $Re = 830$. (*b*) Phase portrait reconstruction using time delays.

figure 10), as illustrated in figure 11(*b*); the opposite is true for MRW$'_\mathrm{A}$. Note that the form of the jets changes substantially near the outer cylinder, so precise quantitative estimates are difficult to make; this is the reason why the jet properties are measured at a fixed radial location $r = r_i + 0.3d$, close to the inner cylinder where the jets are not too distorted by the outer cylinder.

Both MRW$_\mathrm{A}$ and MRW$'_\mathrm{A}$ are relative periodic orbits. Generically, a relative periodic orbit can be expected to become unstable via saddle-node, period-doubling or Hopf bifurcations, but symmetries may result in non-generic dynamics. Specifically, for MRW$_\mathrm{S}$, the space–time symmetry S inhibits period-doubling (Swift & Wiesenfeld 1984), but with MRW$_\mathrm{A}$ this Z_2 symmetry has been broken and the generic behaviour is expected for it. Period-doubling bifurcations (doubling the modulation period τ_m) have been observed experimentally (see curve *PD* in figure 1 and the close-up in figure 9*b*), and have also been detected numerically in the same region of parameter space. As the period-doubling bifurcation is well understood, we focus here on the new dynamics associated with the symmetry-breaking transition between MRW$_\mathrm{S}$ and MRW$_\mathrm{A}$ (curve *PAC* in figure 9*b*).

5.2. *Numerical results near symmetry breaking; jet dynamics and phase space reconstruction*

The numerical simulation of the complex flows we have described allows a more detailed analysis of the flow structure, and of the fine structure associated with the symmetry-breaking transition. However, as we are dealing with very low-frequency modes, with periods going to infinity at the bifurcation, the computation of these three-dimensional complex flows is very expensive, and an extensive exploration of the parameter space is prohibitive. We have analysed in detail a one-dimensional path in parameter space, at $Re = 830$ and varying Γ, crossing the symmetry-breaking bifurcation line. Along this path, we have computed time-series of the axial velocity at mid-gap $(r_i + r_o)/2$ and mid-height $z = 0$, $\hat{W}$, and this quantity has also been measured in the experiments. The resulting time-series include a large periodic component due to the precession frequency of the rotating and modulated rotating waves, which is of a kinematic nature and not dynamically important (Rand 1982; Krupa 1990). Since the modulation frequency ω_m is at least two orders of magnitude smaller than the precession frequency ω_p (as discussed in §4.3 and §5.1), ω_m has been removed by low-pass-filtering $\hat{W}$, giving W. The time-series $W(t)$ for MRW$_\mathrm{S}$ at $\Gamma = 3.16205$ and $Re = 830$ shown in figure 12(*a*) is strictly periodic, and we have rescaled time in seconds for convenient comparisons with the experimental results in §5.4.
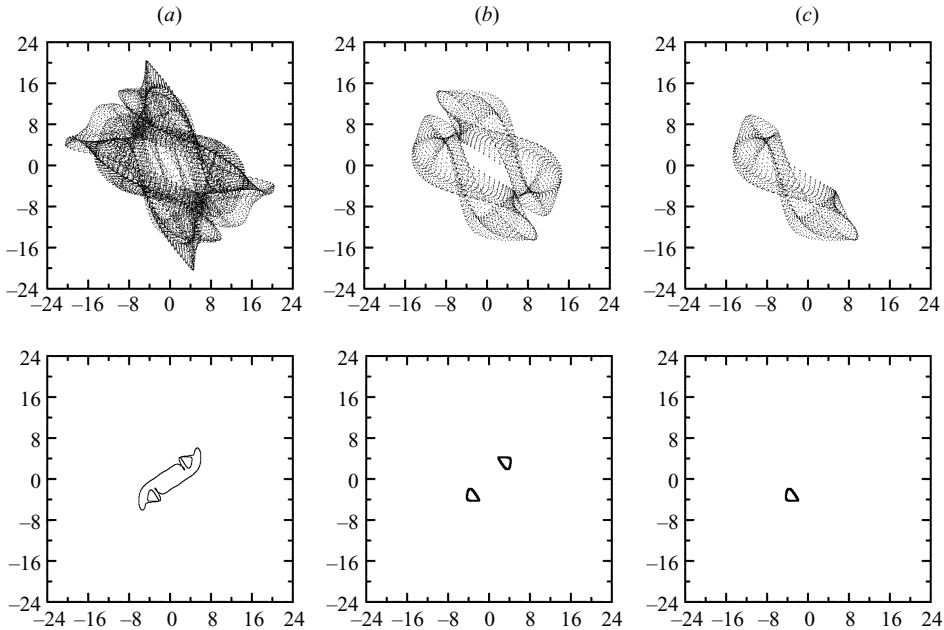
FIGURE 13. Phase-space reconstruction of (*a*) MRW$_S$ at *Re* = 830 and Γ = 3.16205, (*b*) MRW$_A$ and its symmetric MRW$'_A$ at *Re* = 830 and Γ = 3.165, and (*c*) MRW$_A$ on its own at the same *Re* and Γ as in (*b*). The first row is from the computed time-series $\hat{W}(t)$ and the second row corresponds to the low-pass-filtered time-series $W(t)$.

We have also reconstructed phase-space trajectories using time delays, in order to compare with the experimental results. Figure 12(*b*) shows the phase-space reconstruction of the signal in figure 12(*a*), where we have plotted $W(t + t_D)$ against $W(t)$. The (non-dimensional) time delay used in the reconstruction is $t_D = 0.17$, similar to the one used in the reconstruction of the experimental data in § 5.4.

There are a number of ways to suppress the fast precession frequency. One is to apply a low-pass-filter to the time-series (as is done experimentally). This straightforward method is possible because the two frequencies are widely separated (ω_p is two orders of magnitude larger than ω_m). Another way is locally smoothing the time-series, averaging at each point over a temporal interval of the size of the precession period τ_p. Yet another is to use a Poincaré section of the time-series, strobing once every precession period τ_p, or equivalently looking at a fixed location in a reference frame rotating with ω_p. As there are many (topologically equivalent but different) Poincaré sections, we have used the second method (local averaging) which exactly coincides with the low-pass-filtering, and also coincides with one of the Poincaré sections (at a particular phase during the precession period τ_p). The first row in figure 13 shows the phase-space reconstruction of (*a*) MRW$_S$, (*b*) MRW$_A$ and MRW$'_A$ and (*c*) MRW$_A$ on its own, all at *Re* = 830 and Γ as indicated, without filtering out ω_p. The phase-space trajectories densely fill two-tori, corresponding to quasi-periodic solutions with two frequencies. The second row in the figure shows the same phase-space reconstructions, but of the low-pass-filtered time-series, resulting in closed loops (relative periodic orbits). The scale for the plots in the two rows is the same, illustrating the large oscillations corresponding to ω_p (first row), and the small modulations associated with ω_m (second row). The figure clearly exhibits the Z_2 space–time symmetry of MRW$_S$, manifested here as a half-turn symmetry around
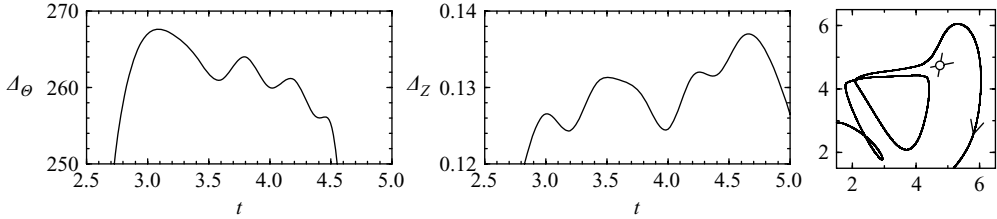
FIGURE 14. Comparison of (*a*) the jets relative phase dynamics Δ_Θ, (*b*) the evolution of the jets intensity Δ_Z, and (*c*) the phase-space reconstruction, for MRW_S at $Re = 830$ and $\Gamma = 3.1616$.

the centre of the phase-space plots, and the symmetrically related characteristics of MRW_A and MRW'_A. It is also evident from the figure that the small loops in the phase-space reconstruction of MRW_S are very close to the phase-space trajectories of MRW_A and MRW'_A.

Figure 14 compares the relative phase dynamics of the jets, described by Δ_Θ and Δ_Z, with the phase-space reconstruction for MRW_S at $Re = 830$ and $\Gamma = 3.1616$. The plots show close-ups of the quiescent phase, where the MRW_S is close to one of the MRW_A. Both the intensity and relative phase of the jets show oscillations during this phase, and these correspond very closely to the loops in phase-space around the MRW_A (small loops in the second row of figure 13). As the symmetry-breaking curve PAC is approached, the number of loops increases and the number of oscillations during the quiescent phase increases accordingly. Therefore, the phase-space reconstructions used in the experiments are directly related to the phase dynamics of the jets.

5.3. *The period-adding cascade and its accumulation point*

The transition between the symmetric oscillations of MRW_S and the non-symmetric oscillations of MRW_A for $Re > 790$ is accomplished via a complex bifurcational process. Figure 15 shows the variation of the modulation period τ_m of the modulated rotating waves in the neighbourhood of the symmetry-breaking bifurcation along the one-dimensional path at $Re = 830$. Instead of a monotonic increase in τ_m going to infinity as would correspond to a blue-sky bifurcation, we observe that MRW_S suffers a cascade of infinite-period bifurcations. As $\Gamma \to 3.1632$ from below, the relative periodic orbit MRW_S executes an increasing number of loops around the ghost of the relative periodic orbits MRW_A and MRW'_A. The switch between executing n and $n + 1$ loops is accomplished by MRW_S undergoing an infinite-period bifurcation. As the number of loops increases, these bifurcations occur for smaller and smaller increments in the parameter Γ. With each extra loop, the modulation period τ_m of MRW_S increases by an approximately constant value (approximately the sum of the modulation periods of MRW_A and MRW'_A). At the accumulation point of this period-adding cascade, both the length and period of the relative periodic orbit MRW_S become infinite and MRW_S is destroyed, leaving MRW_A and MRW'_A at larger Γ.

In order to determine the nature of the sequence of infinite period bifurcations, figure 16 shows close-ups of the phase-space reconstructions around one of the small loops, just before and after the infinite-period bifurcations between n and $n + 1$ loops for $n = 1$ to 7, and just after the accumulation point. The first and last frames show MRW_S and MRW_A solutions away from the bifurcation for comparison purposes. We clearly see that the bifurcations are saddle-loop heteroclinics, where MRW_S
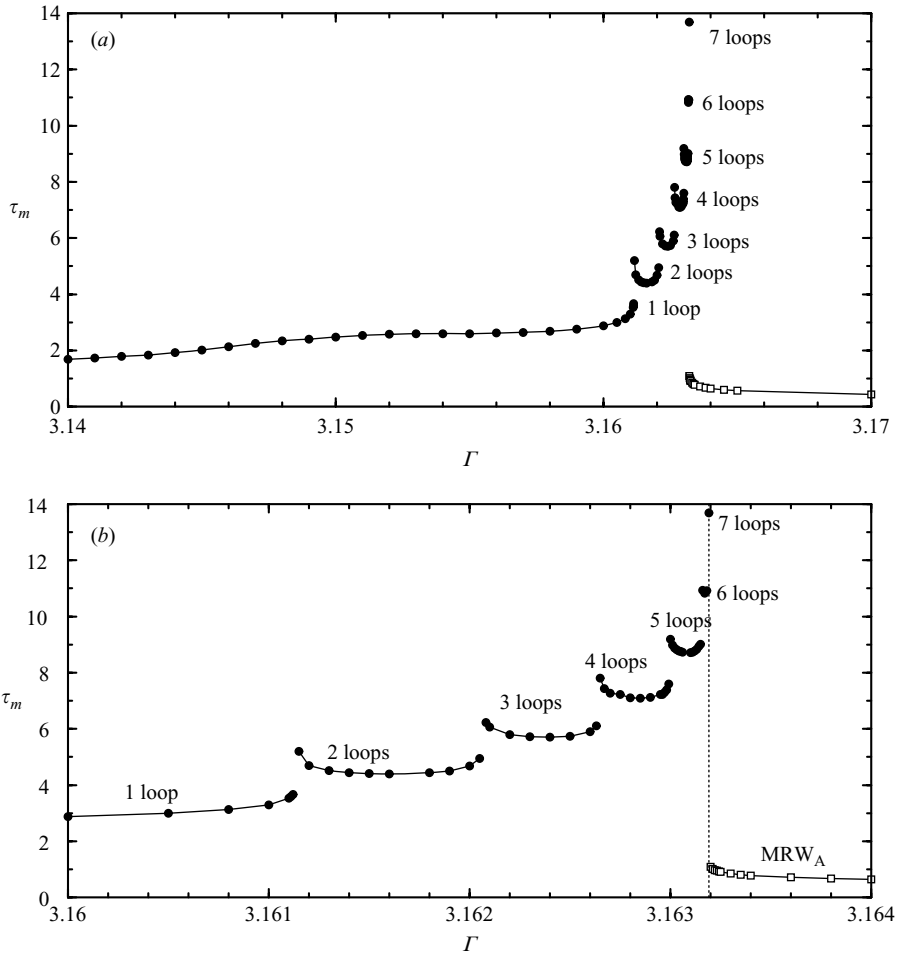
FIGURE 15. Variation with Γ of the modulation periods τ_m of computed stable symmetric relative limit cycles MRW_S (●) and of computed stable pairs of symmetrically related relative limit cycles MRW_A (□) at $Re = 830$; (*b*) is a close up of the period-adding cascade regime in (*a*).

collides with a pair of symmetrically related saddle solutions (only one is shown in the close-ups, indicated by an open circle and short segments of its stable and unstable manifolds). These asymmetric saddle solutions are very likely the RW_A and RW'_A rotating waves. Below $Re = 790$ these solutions were stable, so the collision of MRW_S with them resulted in the *SNIC* bifurcation described previously. Above $Re = 790$, RW_A and RW'_A become unstable at the secondary Hopf bifurcation sH_A. After the collision with the unstable saddle RW_A, the solution trajectory evolves away from RW_A and the space–time Z_2 symmetry S provides the global re-injection mechanism that drives the trajectory towards the symmetrically related saddle RW'_A. These unstable saddles provide a turnstile mechanism that progressively increases the number of loops in a period-adding cascade of saddle-loop heteroclinic bifurcations, culminating in the symmetry-breaking bifurcation point. Approaching the symmetry-breaking bifurcation curve from above in Γ, what we observe in the last three frames is the collision of the stable MRW_A with the saddle RW_A resulting in a saddle-loop
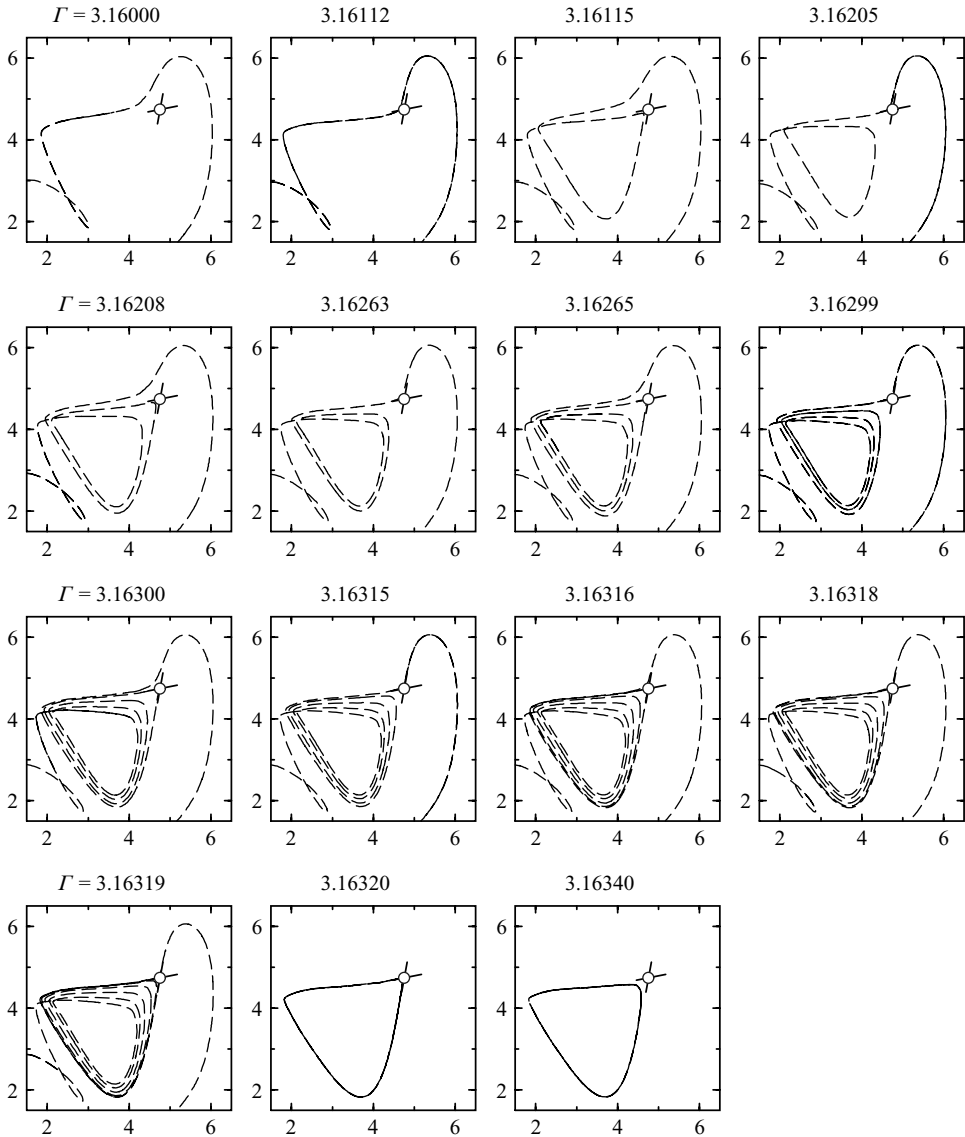
FIGURE 16. Close-ups of the numerical low-pass-filtered projections of MRW_S at $Re = 830$ and Γ as indicated. The saddle RW_A is indicated by an open circle together with segments of its stable and unstable manifolds in this projection.

homoclinic bifurcation where MRW_A ceases to exist; but the presence of the Z_2 symmetry results in the creation of a large loop around both saddles. This large loop is the MRW_S solution that undergoes the inverse period-adding cascade on further decreasing Γ.

A schematic of this dynamics is presented in figure $17(a)$, where the rotating waves are shown as relative equilibria and the modulated rotating waves as relative periodic orbits, as was done in figure $9(a)$. The $+$ signs indicate the number of eigenvalues with positive real part of the relative equilibria RW_S and RW_A. The one-dimensional path γ_2 is shown as a thick arc with an arrow in parameter space in figure $17(b)$.
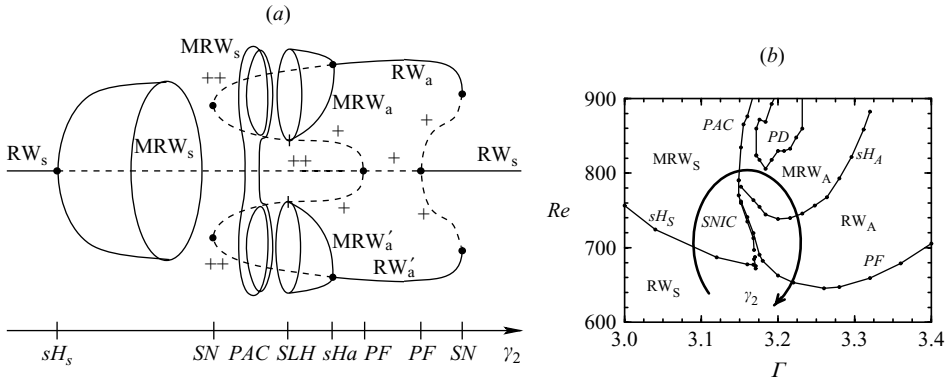
FIGURE 17. Schematic bifurcation diagram for the symmetry-breaking transition involving a period-adding cascade (PAC) of heteroclinic bifurcations culminating in a non-isolated infinite-period catastrophe. The bifurcations indicated are saddle-node (SN), saddle-loop heteroclinic (SLH), secondary Hopf (sH_A) and cyclic pitchfork (PF).
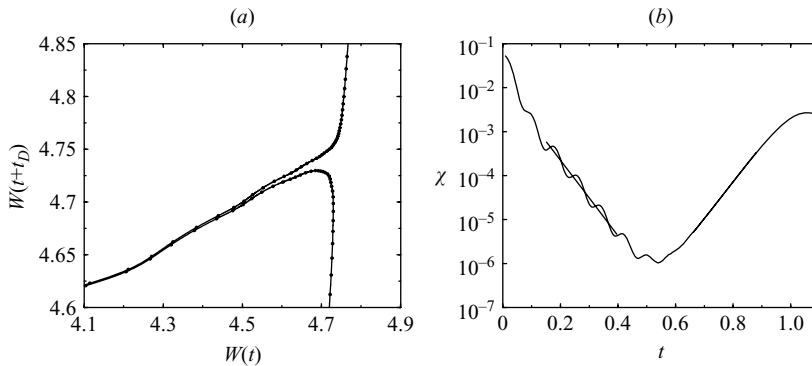

FIGURE 18. (*a*) Detail of the phase-space reconstruction in figure 16 at $\Gamma = 3.16319$ very close to the saddle. (*b*) Plot of $\chi(t)$ corresponding to one of the branches in (*a*); the thick straight lines are a linear fit in the region considered.

MRW$_S$ becomes distorted as it approaches the (unstable) saddles RW$_A$ and RW$'_A$ and experiences repeated heteroclinic collisions with them in the PAC region. These collisions do not modify the stability properties of the saddles. This bifurcation scenario is similar to a blue-sky bifurcation in the sense that the relative periodic orbit has both period and length going to infinity, but it differs in the fact that the blue-sky is an isolated bifurcation, while here the infinite-length and infinite-period bifurcation is the accumulation point of a period-adding cascade of heteroclinic collisions.

As the trajectories of the MRW$_S$ come arbitrarily close to the saddle RW$_A$ at the heteroclinic collisions, the nature of the saddle and its leading eigenvalues can be determined. Figure 18(*a*) shows a detail of the trajectory of MRW$_S$ at $Re = 830$ and $\Gamma = 3.16319$, corresponding to the seven-loop solution in figure 16, very close to the saddle. The solution trajectory enters the stable manifold of the saddle in an oscillatory fashion, indicating that the eigenvalues of the saddle with negative real part closest to the imaginary axis are a pair of complex-conjugate eigenvalues $-\rho \pm i\omega$. On exiting the neighbourhood of the saddle via its unstable manifold, the

trajectory is smooth, corresponding to a single real positive eigenvalue, λ. This is consistent with the schematics in figure 17(a), and suggests that the saddle is of Shil'nikov type. Very close to the saddle the dynamics is completely dominated by the leading eigenvalues of the saddle. In the invariant manifold corresponding to the three leading eigenvalues, the dynamics is very well approximated by the ODE

$$\left. \begin{aligned} \dot{x}_1 &= -\rho x_1 - \omega x_2, \\ \dot{x}_2 &= \omega x_1 - \rho x_2, \\ \dot{x}_3 &= \lambda x_3, \end{aligned} \right\} \tag{5.1}$$

whose general solution is

$$(x_1, x_2, x_3)(t) = (A e^{-\rho t} \cos(\omega t + \delta), A e^{-\rho t} \sin(\omega t + \delta), z_0 e^{\lambda t}), \tag{5.2}$$

where A, δ and z_0 depend on the initial conditions at $t = 0$. Any dynamic variable, such as $W(t)$, will be a linear combination of the above x_i in a neighbourhood of the saddle: $W(t) = \sum_{i=1}^{3} C_i x_i(t) + C_4$. We could try to fit such a function to the curve in figure 18(a), and thus obtain the leading eigenvalues and the C_i. However it is more practical (in order to eliminate the arbitrariness of the origin and the orientations of the axes) to work with the modulus squared of the derivative, $\chi(t) = W'(t)^2 + W'(t + t_D)^2$. A simple computation gives

$$\chi(t) = (A_1 + A_2 \cos(2\omega t + \delta_1)) e^{-2\rho t} + A_3 e^{(\lambda - \rho) t} \cos(2\omega t + \delta_2) + A_4 e^{2\lambda t}. \tag{5.3}$$

Figure 18(b) is a plot of $\chi(t)$ corresponding to a segment of the trajectory in figure 18(a). We observe an exponential decrease in $\chi(t)$ as the saddle is approached, with oscillations, corresponding to the first term in (5.3), and an exponential increase in $\chi(t)$ as the trajectory escapes the saddle, corresponding to the last term in (5.3). A linear fit to these exponential behaviours gives the real parts of the leading eigenvalues: $\rho = 9.878$ and $\lambda = 9.574$. The saddle quantity $\sigma = \lambda - \rho = -0.304$ determines whether the dynamics in the neighbourhood of the saddle is chaotic ($\sigma > 0$) or not ($\sigma < 0$) (see Kuznetsov 2003, chap. 6). In our case $\sigma < 0$ and the heteroclinic collisions do not result in the formation of a chaotic attractor. Generically, such collisions with $\sigma < 0$ only result in the existence of a stable limit cycle that disappears after colliding with the saddle. However our case is not generic due to the symmetries of the problem; the Z_2 symmetry provides a global reinjection mechanism that drives the unstable manifold of the saddle RW_A to the stable manifold of the symmetric-conjugate saddle RW'_A, resulting in a new limit cycle with an extra loop.

Period-adding cascades have been observed and analysed in diverse settings, involving repeated formation and breaking of global connections to a saddle-focus, such as in amplitude-equation models of the Faraday waves problem (Higuera, Porter & Knobloch 2002; Higuera, Knobloch & Vega 2005), and low-dimensional ODE models of semiconductor lasers with optical injection (Yeung & Strogatz 1998; Wieczorek, Krauskopf & Lenstra 2002; Krauskopf & Wieczorek 2002; Krauskopf & Oldeman 2006). However, each of these model problems exhibit different dynamics associated with the period-adding cascade. In the laser examples, the accumulation process is characterized by an infinite series of saddle-node bifurcations of limit cycles. In the Faraday waves model problem, the *PAC* also involves an infinite sequence of saddle-node bifurcations, and each of those bifurcations are symmetry-changing transitions, so that the limit cycle switches from being symmetric to asymmetric to symmetric, and so on, with each period-adding event. In contrast, our *PAC* involves an infinite series of saddle-loop homoclinic bifurcations where on either side of
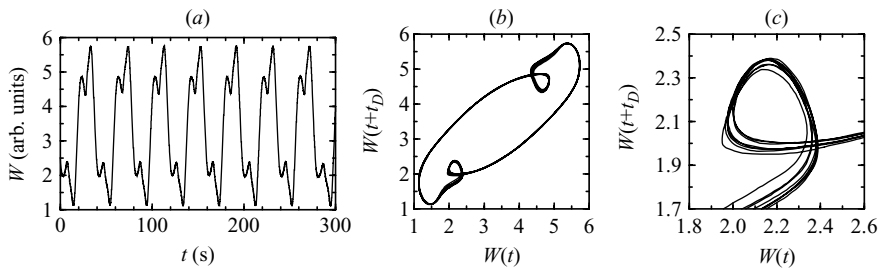
FIGURE 19. (*a*) Low-pass-filtered time-series of the LDV measured axial velocity W for the MRW$_S$ at $\Gamma = 3.1504$ and $Re = 823.3$. (*b*) Phase portrait reconstruction using time delays. (*c*) Close-up of the phase portrait reconstruction.

the *SLH* bifurcation, the limit cycle undergoing the bifurcation exists, is stable, and retains its symmetry; the accumulation point of the *PAC* is the only point of symmetry breaking in the sequence.

Knobloch, Hettel & Dangelmayr (1995) considered a second-order ordinary differential equations model with reflection symmetry in which an infinite cascade of heteroclinic bifurcations occurs in a small parameter regime. While their heteroclinic cascade does not involve limit cycle solutions, and hence is not a *PAC*, it does share with our problem that the cascade involves asymmetric attractors and that the reflection symmetry is restored at the accumulation point.

In many of the aforementioned other examples involving *PAC*, chaotic dynamics have been reported in the neighbourhood of the period-adding event. In the *PAC* studied in this paper, no such chaotic dynamics occur in the numerical simulations (as is expected due to the saddle quantity of the saddle-focus RW$_A$ involved), although the experiments exhibit some erratic behaviour due to the very small drifts in Re, as discussed in § 5.4. However, Lopez & Marques (2005) have previously observed a *PAC* involving Shil'nikov chaos in the analysis of the dynamics associated with the one-jet state, S$_1$, in the Taylor–Couette problem with aspect ratio $\gamma = 4.0$, which is slightly larger than that studied here.

5.4. *Experimental observations near symmetry breaking: intermittency and bursting*

In order to analyse the experimental results close to the symmetry-breaking curve *PAC* shown in figure 17(*b*), a careful analysis of the LDV measurements is needed. Long time-series of the axial velocity at mid-gap $(r_i + r_o)/2$ and mid-height $z = 0$, $\hat{W}$, are recorded using LDV measurements at a fixed angular position $\theta = 0$ in the laboratory reference frame. These time-series include a large periodic component due to the precession frequency of the rotating and modulated rotating waves, that has been removed by low-pass-filtering the LDV signal as it is acquired, giving W, in the same way as in the numerical simulations.

Figure 19(*a*) shows a typical time-series of the low-pass-filtered W for MRW$_S$ at $\Gamma = 3.1504$ and $Re = 823.3$, in arbitrary units corresponding to the LDV signal. The signal $W(t)$ clearly shows the Z_2 space–time symmetry of MRW$_S$, as it makes one oscillation near its maximum value, followed by a rapid excursion to the symmetric values (minima), where it make another oscillation, before jumping back to near the maximum value. In order to better portray this behaviour, a phase-space has been reconstructed using time delays. Figure 19(*b*) shows the phase-space reconstruction of the signal in figure 19(*a*), where we have plotted $W(t + t_D)$ against $W(t)$, and used $t_D = 4$ s. The oscillations near the maximum and minimum of W correspond to

the two small loops in the phase-space plot, and the rapid excursions are the long trajectories connecting them. These oscillations around the small loops correspond to the quiescent time intervals observed in MRW_S when it was close to RW_A at lower Re. At larger Re, MRW_S approaches MRW_A as Γ is increased, and so we observe oscillations in the quiescent phase corresponding to a time evolution close to MRW_A. Recall that MRW_A has a small-amplitude oscillation in Δ_Θ around a mean value away from the $\Delta_\Theta = 180°$ symmetric value . The correspondence between the phase-space trajectories and Δ_Θ (the evolution of the relative phase between the tilts of the jets) has been explored in detail in §5.2.

The comparison of the experimental data in figure 19 and the numerical simulations in figure 12 is very good, the only difference being the units of W (non-dimensionalized axial velocity for the numerics and uncalibrated voltage output from the LDV) and the absence of noise in the simulations. Although the experimental time-series appears periodic, the close-up of the phase trajectories shown in figure 19(c) indicates the presence of experimental noise that makes every loop slightly different from the preceding one.

Figure 20 shows the behaviour of the measured $W(t)$ as the bifurcation curve (labelled PAC in figure 17b) separating symmetric and non-symmetric MRW is approached from the symmetric side. In figures 20(a) and 20(b) time-series and phase portraits of MRW_S for $\Gamma = 3.1600$ are shown, approaching the bifurcation from above, for $Re = 888.3$ and $Re = 879.2$, respectively. There is an increase in the number of turns around the small loops (MRW_A) before the rapid excursions between the opposite loops. This behaviour is much more spectacular in figures 20(c) and 20(d), for $\Gamma = 3.1680$. The number of turns around MRW_A becomes arbitrarily large as the bifurcation curve is approached. On crossing the bifurcation curve, the flow settles down onto either MRW_A or MRW'_A, without any further excursions between the two symmetrically related states. The locations in (Γ, Re)-space of the four experimental observations in figure 20 are shown as $\times$ symbols in figure 21, which shows a close-up of the symmetry-breaking bifurcation curve.

Also, shown as a dashed line in figure 21 is the one-dimensional path in parameter space, at $Re = 830$ and varying Γ, where the numerical simulations in §5.2 and §5.3 have been made. The sequence of infinite-period bifurcations described in figure 15 is shown in parameter space in figure 21 as a sequence of vertical bars on the $Re = 830$ dashed line, accumulating at $\Gamma = 3.1632$. This numerical result compares well with the experimentally determined curve; the difference between the experimental and numerical bifurcation point is about 0.3% in Γ (for fixed Re), or about 5% in Re (for fixed Γ). Considering the experimental uncertainties in the parameters, the experimental difficulty in determining the bifurcation point, the presence of noise and the small imperfection breaking the Z_2 symmetry not included in the numerics, and also the effect of the truncation of the spectral expansion in the simulations, the quantitative agreement is very good.

The reconstructed phase-space trajectories of the MRW_S are closed curves (relative periodic orbits) that develop infinite period and infinite length (due to the arbitrarily many loops around MRW_A and MRW'_A executed each period) as the bifurcation curve is approached. The number of turns around the two small loops in each cycle in the phase portraits shown figure 20 is not constant, but varies in an erratic fashion. The numerical simulations indicate that the observed intermitency and bursting is noise-driven due to the small erratic drifts (below the level of experimental accuracy) in the control parameters (Γ, Re). The numerical simulations, free from noise and imperfections, show strictly periodic and relative periodic solutions for
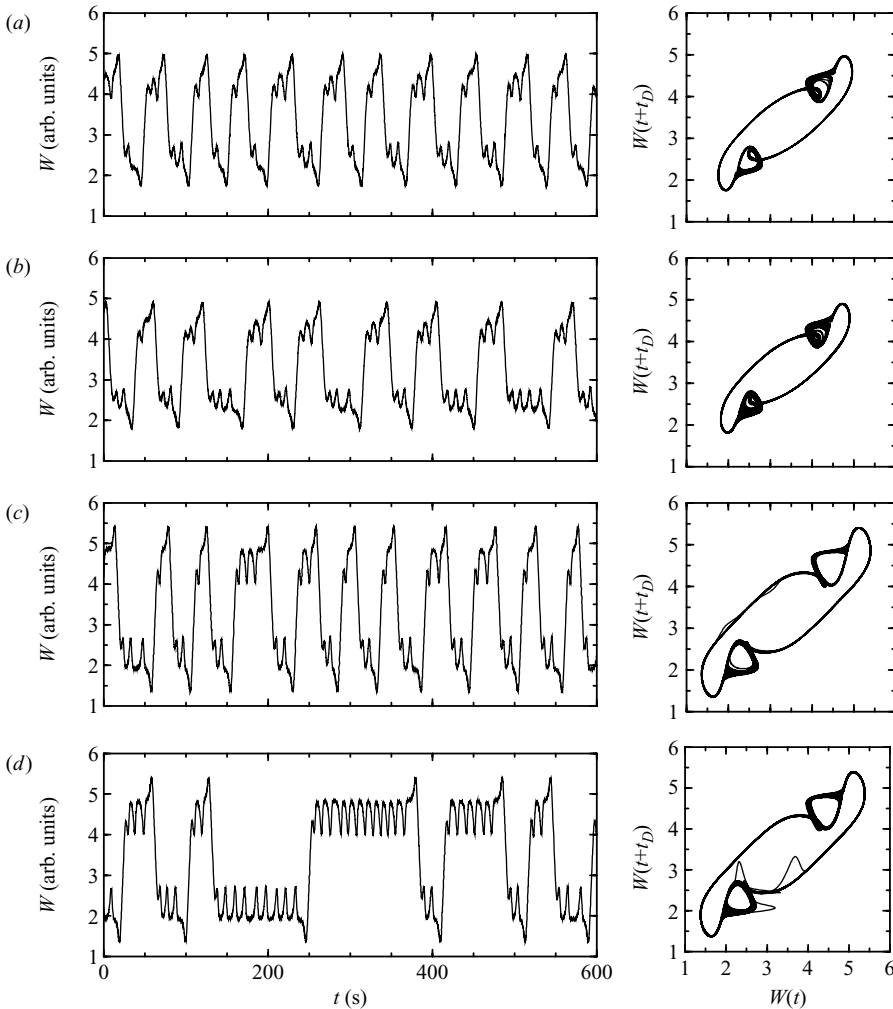
FIGURE 20. Experimental time-series and reconstructed phase portraits for different parameter values. (*a*) $\Gamma = 3.1600$ and $Re = 888.3$; (*b*) $\Gamma = 3.1600$ and $Re = 879.2$; (*c*) $\Gamma = 3.1680$ and $Re = 907.6$; (*d*) $\Gamma = 3.1680$ and $Re = 905.0$.

fixed parameter values (Γ, Re). It is worth mentioning that some of the experimental phase portraits (see figure 20*c*, *d*) show sporadic jumps of the trajectory away from the limit cycle; these are not due to the noise, but due to large isolated perturbations of the experimental apparatus (the experimental runs lasted from several hours up to a few days).

5.5. *Effects of the imperfect Z_2 symmetry*

The time spent close to MRW_A and its symmetric counterpart MRW'_A becomes longer as the symmetry-breaking PAC bifurcation curve is approached. However, in the experiments there is a bias toward MRW_A, around which the solution spends more time than around MRW'_A, and the symmetry-breaking almost always results in an evolution to MRW_A, with the symmetric counterpart MRW'_A being much more difficult to obtain. This corresponds to the presence of some imperfection in the experiment that breaks the reflection symmetry $z \rightarrow -z$ of the apparatus. This small
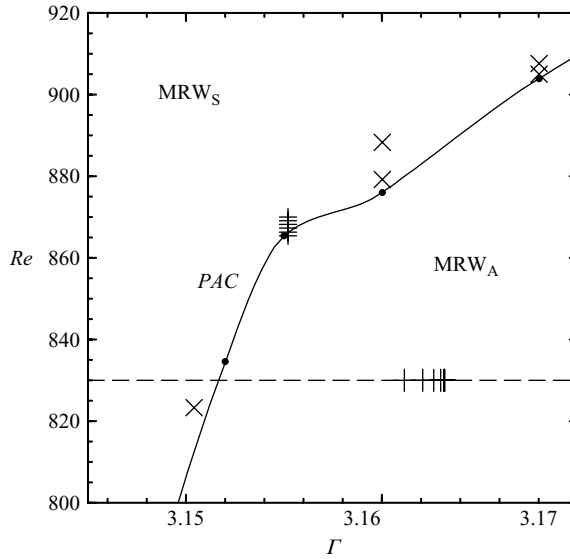
FIGURE 21. Close-up of the symmetry-breaking region (*PAC*) in figure 9(*b*); filled circles correspond to the experimentally determined bifurcation curve, × symbols correspond to the experimental results shown in figures 19 and 20, the sequence of + symbols are the experimental path shown in figure 22. The horizontal dashed line at $Re = 830$ is the one-parameter path explored numerically; the vertical bars on it are the accumulating period-adding sequence discussed in §5.3.

imperfection has been previously reported (Abshagen 2000; Abshagen *et al.* 2005*a*) in other experiments with the same apparatus. Depending on the region in parameter space considered, the effects of the imperfection are more or less pronounced. In figure 20, the asymmetry is not large, although some of the phase portraits show one of the small loops (MRW$_A$) to be more intense (corresponding to spending more time there) than the other (MRW$_A'$). Figure 22 corresponds to approaching the bifurcation curve from above with $\Gamma = 3.1552$ for six different values of Re; the six points are shown in figure 21 as + symbols. Far from the bifurcation point, at $Re = 870.0$, the rapid excursions between MRW$_A$ and MRW$_A'$ (the two small loops) occur very often, and on approaching the symmetry-breaking curve the rapid excursions become more and more sparse, until they finally disappear at the bifurcation curve. The MRW$_S$ has become MRW$_A$; in the last frame at $Re = 865.4$, there is only one rapid excursion observed in one and a half hours (for comparison, the precession period is about 0.46 s).

6. Discussion and conclusions

This study was motivated by the experiments of Abshagen (2000) where the transition between symmetric bursting dynamics and asymmetric regular oscillations resulted in the first experimentally observed bifurcation producing a (relative) periodic orbit of infinite length and period. The natural candidate for such a bifurcation was of blue-sky type, the only isolated bifurcation of limit cycles with infinite length and period. To clarify the details of this novel phenomenon further experiments and numerical simulations have been conducted, revealing the transition to be more complicated than an isolated blue-sky bifurcation. Instead, it is a non-isolated
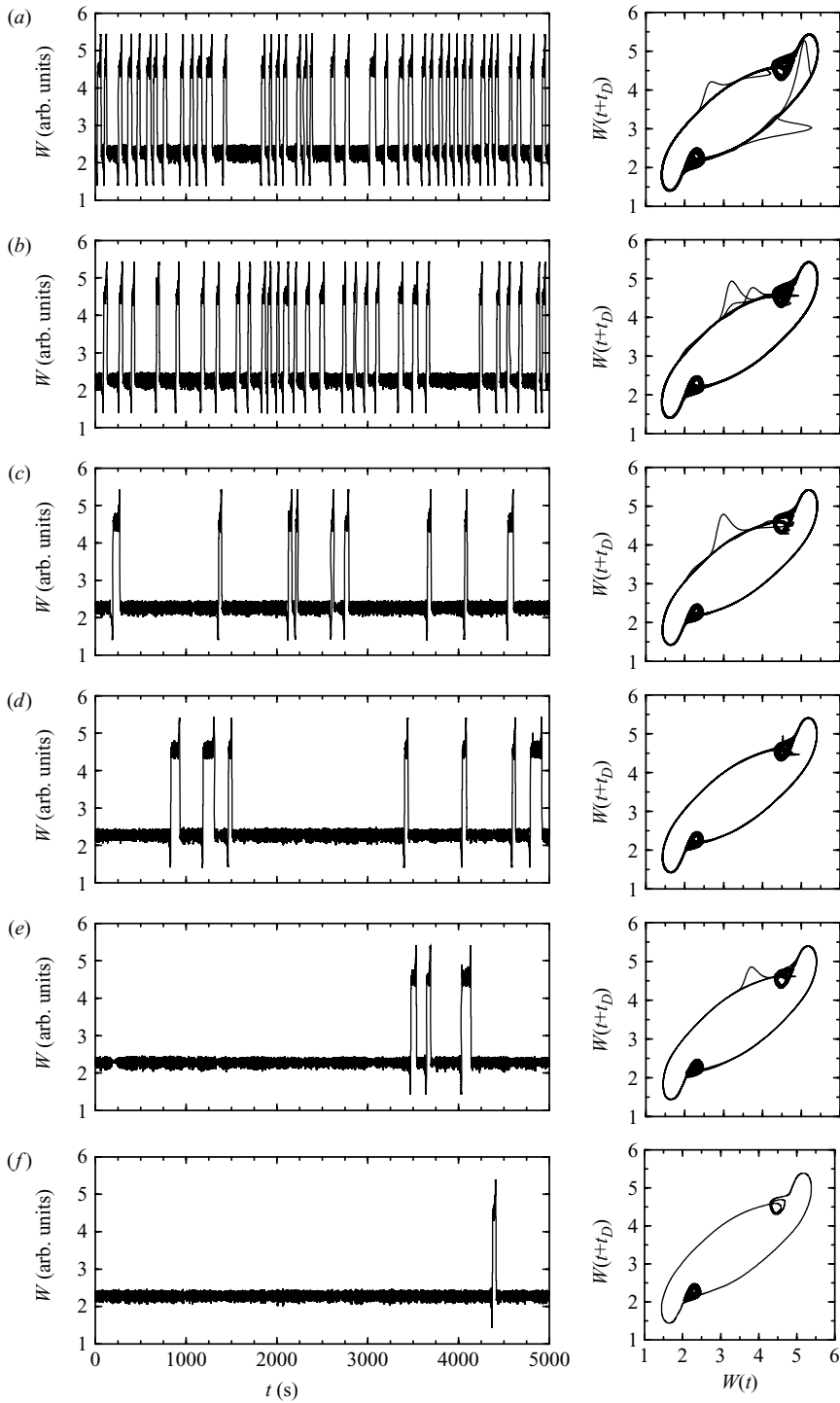
FIGURE 22. Experimental time-series and reconstructed phase portraits of bursting solutions for $\Gamma = 3.1552$ and decreasing Re values. (*a*) $Re = 870.0$; (*b*) $Re = 869.1$; (*c*) $Re = 868.2$; (*d*) $Re = 867.3$; (*e*): $Re = 866.3$; (*f*): $Re = 865.4$.

infinite-period and infinite-length bifurcation, involving a period-adding cascade of saddle-loop heteroclinic bifurcations.

In the neighbourhood of the accumulation point of the period-adding cascade, as the number of loops increases, the saddle-loop heteroclinic bifurcations occur for smaller and smaller increments in the parameter, and the effects of noise (e.g. due to changes in Re induced by small temperature fluctuations) results in a drift of the governing parameters leading to experimental time-series showing states with different numbers of loops, as illustrated in figures 20 and 22. Although the solutions at fixed values of the parameters are relative periodic orbits, they appear chaotic in the experiments due to the parameter drifts caused by the unavoidable presence of noise. Nevertheless, there is very close agreement between the computed and experimental results, even very close to the accumulation point, as is illustrated by comparing the phase portraits from experimental data in figures 20 and 22 with the numerically obtained phase portraits in figures 12 and 16.

The physical flow feature associated with the loops is the azimuthal oscillations of the jets we have observed in MRW_A (figure 10). Each small loop in a MRW_S solution corresponds to a full azimuthal oscillation of MRW_A. The excursions between loops correspond to rapid excursions between MRW_A and MRW'_A, manifested as large jumps in the relative phase of the jets Δ_Θ, and in an axial oscillation of the jets: the jet with the larger (smaller) axial span becomes the jet with smaller (larger) axial span. This interchange is due to the action of the Z_2 symmetry. During half of the MRW_S modulation period, the solution resembles MRW_A, while during the other half-period it resembles the Z_2-conjugate MRW'_A. This is clearly seen in the one-loop solution shown in figures 6 and 7 as well as in the schematic bifurcation diagram in figure 17.

The dynamics associated to the fast time scale is simple (a periodic precession due to $SO(2)$ symmetry-breaking, whose dynamics are completely decoupled), and the interesting dynamics including the period-adding cascade occurs in the slow-varying variables associated with the phase dynamics of the tilted jets. The phenomenon is robust, as shown by the detailed agreement between the numerical simulations and the physical experiments with their inherent imperfections and noise.

While local linear stability analysis accounts for the first few bifurcations and fully blown turbulence may be analysed using asymptotics, neither of these approaches is applicable to the transition bifurcational process we have found. The nonlinear dynamics approach provides a means for characterizing and gaining some understanding of the transition. The Z_2 symmetry seems to be central in providing the system with the global re-injection mechanisms in the *SNIC* bifurcation and the heteroclinic period-adding cascade. These complex dynamics are not easy to analyse, either from the experimental or numerical points of view. Nevertheless, even at large Reynolds numbers, we have shown that the flow behaviour can be captured by using fundamental ideas from dynamical systems theory.

REFERENCES

ABSHAGEN, J. 2000 Organisation chaotischer Dynamik in der Taylor-Couette-Strömung. PhD thesis, University of Kiel.

ABSHAGEN, J., LOPEZ, J. M., MARQUES, F. & PFISTER, G. 2005*a* Mode competition of rotating waves in reflection-symmetric Taylor-Couette flow. *J. Fluid Mech.* **540**, 269–299.

ABSHAGEN, J., LOPEZ, J. M., MARQUES, F. & PFISTER, G. 2005*b* Symmetry breaking via global bifurcations of modulated rotating waves in hydrodynamics. *Phys. Rev. Lett.* **94**, 074101.

ABSHAGEN, J., PFISTER, G. & MULLIN, T. 2001 Gluing bifurcations in a dynamically complicated extended flow. *Phys. Rev. Lett.* **87**, 224501.

BENJAMIN, T. B. 1978*a* Bifurcation phenomena in steady flows of a viscous fluid. I. Theory. *Proc. R. Soc. Lond.* A **359**, 1–26.

BENJAMIN, T. B. 1978*b* Bifurcation phenomena in steady flows of a viscous fluid. II. Experiments. *Proc. R. Soc. Lond.* A **359**, 27–43.

BENJAMIN, T. B. & MULLIN, T. 1981 Anomalous modes in the Taylor experiment. *Proc. R. Soc. Lond.* A **377**, 221–249.

CRAWFORD, J. D. & KNOBLOCH, E. 1991 Symmetry and symmetry-breaking bifurcations in fluid dynamics. *Annu. Rev. Fluid Mech.* **23**, 341–387.

GERDTS, U., VON STAMM, J., BUZUG, T. & PFISTER, G. 1994 Axisymmetric time-dependent flow in the Taylor-Couette system. *Phys. Rev.* E **49**, 4019–4026.

GUCKENHEIMER, J. 1984 Multiple bifurcation problems of codimension two. *SIAM J. Math. Anal.* **15**, 1–49.

GUCKENHEIMER, J. & HOLMES, P. 1997 *Nonlinear Oscillations, Dynamical Systems, and Bifurcations of Vector Fields*. Springer.

HIGUERA, M., KNOBLOCH, E. & VEGA, J. M. 2005 Dynamics of nearly inviscid Faraday waves in almost circular containers. *Physica* D **201**, 83–120.

HIGUERA, M., PORTER, J. & KNOBLOCH 2002 Heteroclinic dynamics in the nonlocal parametrically driven nonlinear Schrödinger equation. *Physica* D **162**, 155–187.

KNOBLOCH, E., HETTEL, J. & DANGELMAYR, G. 1995 Parity breaking bifurcation in inhomogeneous system. *Phys. Rev. Lett.* **74**, 4839–4842.

KNOBLOCH, E. & MOEHLIS, J. 1999 Bursting mechanisms for hydrodynamical systems. In *Pattern Formation in Continuous and Coupled Systems: A Survey Volume* (ed. M. Golubitsky, D. Luss & S. H. Strogatz), pp. 157–174. Springer.

KRAUSKOPF, B. & OLDEMAN, B. E. 2006 Bifurcations of global reinjection orbits near a saddle-node Hopf bifurcation. *Nonlinearity* **19**, 2149–2167.

KRAUSKOPF, B. & WIECZOREK, S. 2002 Accumulating regions of winding periodic orbits in optically driven lasers. *Physica* D **173**, 97–113.

KRUPA, M. 1990 Bifurcations of relative equilibria. *SIAM J. Math. Anal.* **21**, 1453–1486.

KUZNETSOV, Y. A. 2003 *Elements of Applied Bifurcation Theory*, 3rd edn. Springer.

LOPEZ, J. M. & MARQUES, F. 2003 Small aspect ratio Taylor-Couette flow: Onset of a very-low-frequency three-torus state. *Phys. Rev.* E **68**, 036302.

LOPEZ, J. M. & MARQUES, F. 2005 Finite aspect ratio Taylor-Couette flow: Shil'nikov dynamics of 2-tori. *Physica* D **211**, 168–191.

LOPEZ, J. M., MARQUES, F. & SHEN, J. 2002 An efficient spectral-projection method for the Navier-Stokes equations in cylindrical geometries II. Three dimensional cases. *J. Comput. Phys.* **176**, 384–401.

LOPEZ, J. M., MARQUES, F. & SHEN, J. 2004 Complex dynamics in a short Taylor-Couette annulus with the top endwall stationary and the bottom rotating. *J. Fluid Mech.* **501**, 327–354.

LOPEZ, J. M. & SHEN, J. 1998 An efficient spectral-projection method for the Navier-Stokes equations in cylindrical geometries I. Axisymmetric cases. *J. Comput. Phys.* **139**, 308–326.

MARQUES, F. & LOPEZ, J. M. 2006 Onset of three-dimensional unsteady states in small-aspect-ratio Taylor-Couette flow. *J. Fluid Mech.* **561**, 225–277.

MARQUES, F., LOPEZ, J. M. & IRANZO, V. 2002 Imperfect gluing bifurcation in a temporal glide-reflection symmetric Taylor-Couette flow. *Phys. Fluids* **14**, L33–L36.

MECA, E., MERCADER, I., BATISTE, O. & RAMIREZ-PISCINA, L. 2004 Blue sky catastrophe in double-diffusive convection. *Phys. Rev. Lett.* **92**, 234501.

MOEHLIS, J. & KNOBLOCH, E. 1998 Forced symmetry breaking as a mechanism for bursting. *Phys. Rev. Lett.* **80**, 5329–5332.

MULLIN, T. 1993 *The Nature of Chaos*. Oxford University Press.

PALIS, J. & PUGH, C. 1974 Fifty problems in dynamical systems. In *Dynamical Systems – Warwick, 1974* (ed. A. Manning), Lecture Notes in Mathematics, vol. 468, pp. 345–353. Springer.

RAND, D. 1982 Dynamics and symmetry. Predictions for modulated waves in rotating fluids. *Arch. Rat. Mech. Anal.* **79**, 1–38.

SHIL'NIKOV, L. & TURAEV, D. 2000 A new simple bifurcation of a periodic orbit of blue sky catastrophe type. In *Methods of Qualitative Theory of Differential Equations and Related Topics* (ed. L. S. L. Lerman, G. Polotovskii). AMS Transl. Series II, vol. 200, pp. 165–188. AMS.

SHIL'NIKOV, L. P., SHIL'NIKOV, A. L., TURAEV, D. V. & CHUA, L. O. 2001 *Methods of Qualitative Theory in Nonlinear Dynamics. Part II*. World Scientific.

SHIL'NIKOV, L. P. & TURAEV, D. V. 1997 Simple bifurcations leading to hyperbolic attractors. *Computers Math. Applic.* **34**, 173–193.

VON STAMM, J., GERDTS, U., BUZUG, T. & PFISTER, G. 1996 Symmetry breaking and period doubling on a torus in the VLF regime in Taylor-Couette flow. *Phys. Rev. E* **54** (5), 4938–4957.

SWIFT, J. W. & WIESENFELD, K. 1984 Suppression of period doubling in symmetric systems. *Phys. Rev. Lett.* **52**, 705–708.

TURAEV, D. V. & SHIL'NIKOV, L. P. 1995 On blue sky catastrophies. *Doklady Akademii Nauk* **342**, 596–599.

WIECZOREK, S., KRAUSKOPF, B. & LENSTRA, D. 2002 Multipluse excitability in a semiconductor laser with optical injection. *Phys. Rev. Lett.* **88**, 063901.

YEUNG, M. K. S. & STROGATZ, S. H. 1998 Nonlinear dynamics of a solid-state laser with injection. *Phys. Rev. E* **58**, 4421–4435.